Astron. Astrophys. 327, 671–680 (1997)

ASTRONOMY AND ASTROPHYSICS

Sub-arcsecond morphology and kinematics of the DG Tauri jet in the [O I]λ6300 line*

Claudia Lavalley[1], **Sylvie Cabrit**[2], **Catherine Dougados**[1], **Pierre Ferruit**[3], **and Roland Bacon**[3]

[1] Laboratoire d'Astrophysique, Observatoire de Grenoble, UMR CNRS 5571, Université Joseph Fourier, B.P.53X, F-38041, Grenoble Cedex 9, France
[2] Observatoire de Paris, DEMIRM, URA 336 du CNRS, 61 Avenue de l'Observatoire, F-75014 Paris, France
[3] Observatoire de Lyon, UMR CNRS 5574, 9, av. Charles André, F-69561 Saint-Genis-Laval Cedex, France

Received 27 June 1996 / Accepted 5 May 1997

Abstract. We present the first 3D spectro-imaging observations of the [O I]λ6300 line in an active T Tauri star: DG Tau. The morphological structure of the mass outflow is revealed with unprecedented spatial resolution (0.35″). It consists of an unresolved inner peak containing two thirds of the total line flux, followed by a collimated jet-like body extending out to $\sim 1.5''$ from the star, and two resolved knots at distances of 2.7″ and 4″. One of the outer knots possesses a curved morphology and transverse velocity gradient strongly suggestive of a resolved bowshock. Time variability in the ejection velocity (with timescale $\Delta t \simeq 8.5$ yr) could explain the presence of such a bowshock, the spacing of knots at distances $\geq 1''$ from the star, and the strong velocity gradients along the jet observed closer to the star. The unresolved inner peak, centered at ∼20 AU of the star, is apparently stationary and possibly linked to the initial jet collimation. Our size limit and absolute photometry for this peak set new constraints on the jet mass loss rate (between 1.3×10^{-8} and 6.5×10^{-6} $M_\odot$ yr^{-1}), lowering previous estimates by a factor 5 to 25. Finally, our high sensitivity combined with velocity information allows us to detect unambiguously the counterjet of the system ($v \simeq +230$ km/s), and to establish the existence of a diffuse halo of low-velocity [O I] emission, which might trace a wider flow or an extended scattering nebula.

Key words: stars: pre-main sequence – stars: mass-loss – ISM: jets and outflows – stars: individual: DG Tau

1. Introduction

The bipolar outflow phenomenon plays a fundamental role at all early stages of stellar evolution, from the most deeply embedded protostars to optically revealed young low-mass stars (e.g. Edwards et al. 1993). In optically visible T Tauri stars (hereafter TTS), the blueshifted, optically thin forbidden lines of weakly ionized atoms such as [O I],[S II],[N II] provide a unique probe of heated regions of the innermost parts of the stellar wind (Jankovics et al. 1983; Appenzeller et al. 1984; Edwards et al. 1987). Their study reveals that ejection is intrinsically linked with accretion onto the star (Cabrit et al. 1990; Hartigan et al. 1995, hereafter HEG95). However the exact nature of this link and the ejection mechanism still need to be elucidated. This requires determining the heating mechanism for the forbidden line emission, as well as the geometry and kinematic structure of the wind.

High-resolution spectra of forbidden lines in TTS (Edwards et al. 1989; HEG95) show two velocity components of distinct properties and origins: A fast ($v \simeq -200$ km/s) component of relatively high excitation, and a low velocity ($v \simeq -10$ km/s) component of lower excitation and higher density, suggested to originate in an intrinsically slower disk wind (Kwan & Tademaru 1988, 1995; HEG95). The spatial structure of these components at scales ~ 0.1–$1''$ can be retrieved through spectro-imaging, which allows precise subtraction of the stellar continuum, as first demonstrated by Solf (1989) using long-slit spectra. Long-slit studies suggest that the high-velocity component of forbidden lines is formed in a spatially extended and collimated jet, while the low-velocity component is much more compact (Solf & Böhm 1993, hereafter SB93; Böhm & Solf 1994; Solf 1994; Hirth et al. 1994). Clearly, extending such studies to two spatial dimensions is essential to further clarify the formation of forbidden lines in T Tauri stars, and to obtain direct information on the collimation, time variability, and mass flux in their jets, which would set firmer constraints on the ejection mechanism.

DG Tau is a favorable target for such a detailed study, as it is one of the strongest forbidden line emitters among TTS. SB93 inferred indirectly the presence of a jet from long slit spectra at various orientations, and found a complex structure along the jet axis, with at least 3 components of differing density, excitation, and velocity behavior. However, the absence of

Send offprint requests to: Claudia Lavalley

* Based on observations collected at the Canada-France-Hawaii Telescope, operated by the National Research Council of Canada, the Centre National de la Recherche Scientifique, and University of Hawaii.

information transverse to the jet restricts possible physical interpretation. High angular resolution narrow-band imaging in [O I]λ6300 and Hα with the HST by Kepner et al. (1993) also indicated the existence of a jet, already collimated at a projected distance of ∼40 AU from the star. However, these images were obtained prior to HST repair and thus suffer from a very poor PSF. In addition, they do not provide information on the kinematics of the emission. Until now, no combined 3D-spatial *and* spectral information was available.

We present here the first spectro-imaging study of DG Tau, performed in the [O I]λ6300 line with the instrument TIGER at CFHT (Sect. 2). The combination of high angular resolution (0.4″) and moderate spectral resolution (170 km/s) allows us to probe for the first time the two-dimensional morphology and basic kinematics of the mass outflow (Sect. 3). The detailed structure of the blueshifted jet is interpreted in Sect. 4. Sect. 5 and 6 discuss the faint counter-jet and the halo component discovered in our data. Sect. 7 summarizes our conclusions.

2. Observations and data reduction

Observations of DG Tau were made on November 3rd 1994 at the Canada-France-Hawaii (CFHT) 3.60m telescope using the TIGER spectro-imager developed at Observatoire de Lyon. Bi-dimensional spatial sampling of the field of view is achieved with an hexagonal compact array of circular microlenses. The small exit micropupil of each lens is then dispersed with a grism, providing a series of 450 spectra onto the CCD. A detailed description of the instrument can be found in Bacon et al. (1995).

The spatial sampling is 0.4″ per lens and the spectral sampling 1.5 Å/pixel (71 km/s) providing a wavelength coverage of 200 Å and a velocity resolution of 3.4Å =170 km/s at 6300Å. Three frames were taken (300, 1800 and 1800 seconds). They were later co-added in order to increase the signal to noise ratio and improve spatial sampling. The final data array is an irregular grid with spacings between 0.2″ and 0.4″ .

Data reduction was completed using a dedicated reduction software. This reduction consisted in electronic bias substraction, flat-field correction and spectra extraction, wavelength and flux calibration, cosmic ray removal. A full description of the standard procedures can be found in Rousset (1992).

Division by the spectrum of the early type (A2) reference star HD2857, observed within an hour and a half of DG Tau, provided both photometric calibration and correction for the telluric H_2O absorption lines. Air mass correction is included in this procedure. The night sky [O I] emission line profile was determined as the median of spectra free of source signal. A gaussian fit to this unresolved profile (with peak intensity 2×10^{-19} W m^{-2} Å^{-1} arcsec^{-2} and centroid velocity -8 km/s) was then subtracted from all spectra. Comparison of the sky line centroid at various positions across the array shows that the absolute velocity calibration is accurate to within ± 10 km/s (3σ).

Final spectra are calibrated in flux-units of 10^{-19} W m^{-2} Å^{-1} arcsec^{-2} and velocities are expressed in the stellar rest frame.

3. General results

3.1. Integrated [O I]λ6300 line and continuum images

The left panel of Fig. 1 displays the two dimensional images of the continuum and continuum-subtracted [O I]λ6300 line intensity towards DG Tau as derived from our data. Continuum level was determined at each lens position through a second order polynomial fit (excluding the [O I]λ6300,6363 doublet). The [O I]λ6300 line and continuum intensities were then obtained by integration over 40Å. In these and all following images, the original grid of lenses is resampled onto a rectangular grid with 0.133″ spacing.

The continuum image appears unresolved (FWHM ∼ 0.75″). In contrast, the line map is clearly extended along PA=222°, confirming the jet orientation inferred by SB93 (PA 226°), and giving for the first time direct access to the two dimensional morphology of the jet within 4″ of the star.

Since the continuum and the line were recorded simultaneously, and the wavelength range is sufficiently small that the PSF can be considered as independent of λ, we can further enhance spatial resolution by deconvolving the [O I] map by the continuum image. We use the LUCY-Richardson algorithm as implemented in the STSDAS package of the IRAF software. A subsection of the continuum image is used as an estimate of the PSF. Using a two-dimensional gaussian fit to the continuum did not significantly improve the results . Convergence is achieved in typically 20 iterations and results in an improved angular resolution of 0.35 ″ as determined from the FWHM of the inner [O I] peak, which is expected to be unresolved (SB93). The deconvolved image is shown in the right panel of Fig. 1. The same basic features are retrieved when using a maximum entropy deconvolution method.

The observed [O I] emission (see Fig. 1) along the DG Tau jet has a complex morphology with the following features:

- A main peak slightly displaced from the continuum (a two dimensional gaussian fit yields a displacement of 0.17″ ± 0.05″ in the raw image, 0.13″ in the deconvolved one).
- A fainter jet-like elongation extending out to 1.5″ from the star, marginally resolved perpendicular to the jet axis (cf. Sect. 4.2).
- A separate knot at ∼ 2.6″ clearly transversally resolved, with a striking bow geometry.
- A faint outermost knot at ∼ 4″ , also resolved transversally but with signal to noise ratio too low to define its geometry.

We thus witness a clear morphological evolution of the [O I] emission, from a collimated jet-like body at distances ≤ 1.5″ from the star, to a series of discrete extended knots in the outer regions. In addition, Fig. 1 reveals two previously unreported regions of [O I] emission towards DG Tau: (1) A peak and fainter wings towards the north-east of the star, shown below to trace a counter-jet, (2) A faint halo in the raw [O I] image in regions well outside the body of the jet, not seen in the continuum. This halo is too faint and diffuse to be retrieved in the deconvolved map.

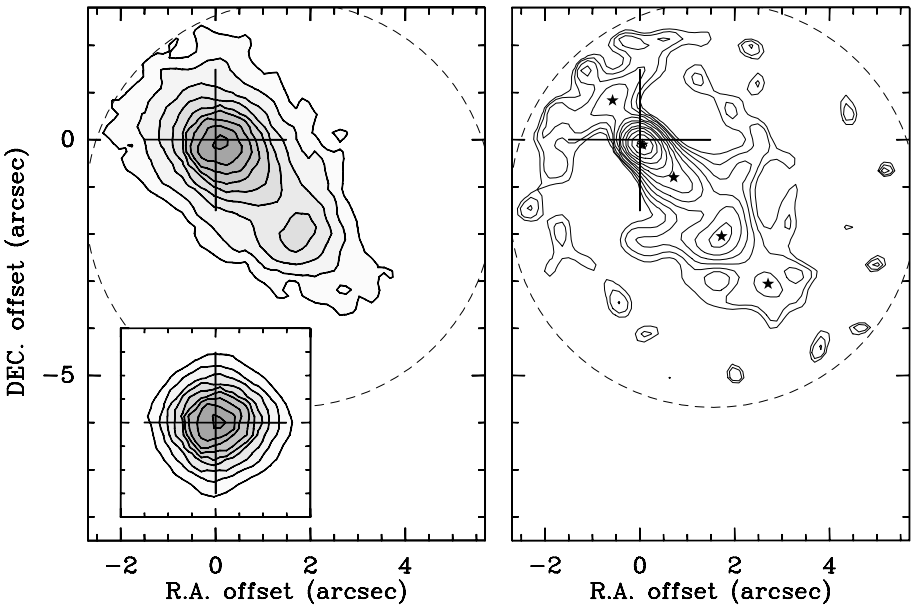

Fig. 1. Subarcsecond images of DG Tau in the [O I]λ6300 line. Left panel: continuum-subtracted [O I] integrated intensity, with the continuum shown as insert. Effective resolution is 0.75″ . Right panel: same [O I] map after deconvolution by the continuum. Effective resolution is 0.35″ . Contours decrease by factors of 2 starting at 83 % of the peak (lowest contour at $\sim 4\sigma$ for the line map). Peak values are 5.8 10^{-16} W m^{-2} arcsec^{-2} in the raw [O I] image and 3.6 10^{-15} W m^{-2} arcsec^{-2} in the continuum. Stars mark distinct emission structures in the jet (see text). The dashed circle shows the edge of our field of view.

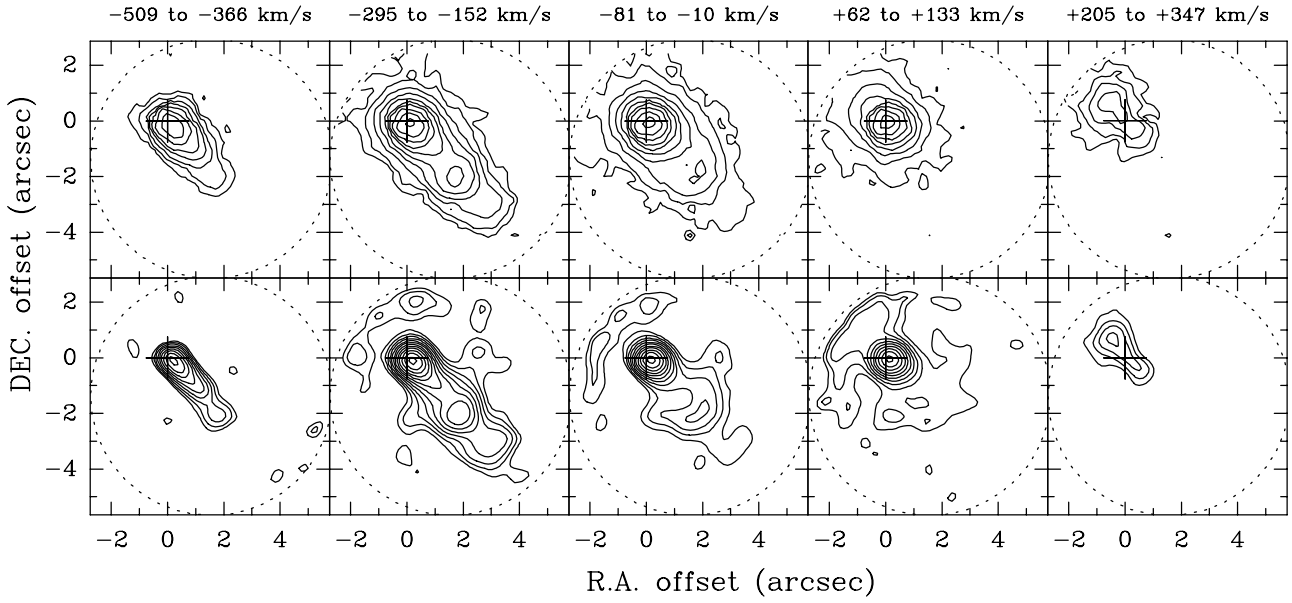

Fig. 2. Upper panels: channel maps with central velocity ranging from highly blueshifted (−430 km/s) at left, to highly redshifted (+270 km/s) at right. Velocity ranges (covering 2 or 3 individual spectral channels) are indicated at the top of each panel. Contours increase by factors of 2, starting at 3.6×10^{-19} W m^{-2} arcsec^{-2} ($\sim 4\sigma$). Bottom row: same channels after Lucy-Richardson deconvolution by the continuum (resolution $\sim 0.5''$), with contours starting at 83% of the peak. The dotted circle shows the edge of our field of view.

3.2. Global kinematics

3.2.1. Channel maps and line profiles

We first investigate the global two-dimensional kinematical information provided by our data using channel maps (Fig. 2) and representative line profiles (Fig. 3). Inspection of these figures reveals that:

(1) Highly redshifted emission is present towards the north-east (cf. rightmost panel of Fig. 2), suggesting that we have detected the counter-jet of the system. This is unambiguously confirmed by the average line profile (top panel of Fig. 3), which shows a distinct redshifted spectral component at $\sim$ +230 km/s not present towards other regions. Note that the redshifted emission observed towards the south-west corresponds to faint line wings from a bright low-velocity blueshifted component (cf. middle panels of Fig. 3).

(2) Blueshifted emission is essentially confined to the main peak and the jet towards the south-west, as expected. Strong velocity variations occur along the jet, as first found by SB93. The central unresolved knot dominates at all velocities below

−300 km/s. The corresponding line profile shows a low-velocity peak at ∼ −50 km/s, with an extended blue wing (Fig. 3). At higher velocities, the emission peaks further out from the continuum, towards the jet-like extension. The line profile in that region reflects this velocity increase, with a peak now shifted to ∼ −300 km/s, and a low-velocity shoulder around ∼ −150 km/s. Velocity and line width then decrease towards the outer two knots. Corresponding line profiles are narrow (FWHM < 250 km/s) and peak at moderate velocities (∼ −200 km/s), with a faint low-velocity wing (bottom panel of Fig. 3). In this region, the jet appears wider at low velocity, suggesting a velocity gradient perpendicular to the jet axis, which will be investigated in Sect. 4.2.

(3) The faint halo is associated with a broad spectral feature visible in our channel maps from −100 km/s to +100 km/s. Line profiles peak at low velocity (∼ −50 to 0 km/s). The emission structure and line profile of this component are discussed in detail in Sect. 6 and Fig. 6.

3.2.2. Gaussian fits

Despite our medium spectral resolution which prevents us from obtaining the detailed velocity structure observed by SB93, our spectra are still asymmetric and well resolved in width (FWHM ≥ 250 km/s) out to 2″ from the star (Fig. 3), indicating several underlying velocity components. To evaluate in a quantitative way the line centroids, we apply a gaussian fitting procedure to the line profiles. We stress that the results of these fits will be used essentially to illustrate the overall velocity gradients in the blueshifted jet. In addition, the fits will allow us to better define the centroid velocity of weak features such as the red counter-jet and the halo.

To avoid restrictive a-priori assumptions on the velocity ranges, we first explored the full parameter space (V between −350 and +350 km/s, FWHM from 3–10Å) for several representative spectra; we found that the absolute minimum χ^2 is reached for fits that include one "low-velocity" gaussian (LV), ranging in velocity from −185 km/s (at the tip of the jet-like extension) to 25 km/s (in the counter-jet), and one "high-velocity" gaussian (HV), either blueshifted in the jet and halo (V ∼ −350 to −165 km/s), or redshifted in the counter-jet (V ∼ +215 km/s to 340 km/s). To speed up the minimum χ^2 search over our full datacube, we then start the iteration with 3 gaussian components, restricting their centroid velocity to vary inside the expected ranges: −350 to −150 km/s (HVB), −190 to +150 km/s (LV), +150 to +350 km/s (HVR). The intervals for the FWHM are 3.5–7 Å for the HVR and LV, 3.5–8 Å for the HVB. Two of these components at most contribute significantly to the flux at each spatial position.

Uncertainties in the fitting procedure depend strongly on the separation between the two components and on their S/N ratio. Based on a study of simulated noisy profiles built up from two gaussians, we only consider fit results for profiles with S/N ≥ 10 on the total line peak and S/N ≥ 5.5 on each kinematical component. Typical uncertainties (1σ) are then ± 20 km/s on the centroid velocity and 15% on the integrated line flux of each component, for a FWHM of the total profile ≥ 250 km/s. For narrower profiles, uncertainties in velocities and intensities increase significantly. We chose in that case to fit a single gaussian, which gives an adequate description of the profile. Our derived uncertainties are fully confirmed by a study of the χ^2 space near minimum in representative spectra (Bevington 1969). Examples of our gaussian fits and their residuals are shown in Fig. 3.

Table 1. Left: Distance from continuum, centroid velocities, and dereddened [O I]λ6300 luminosities of the emission features in the DG Tau jet. Right: Equivalent structures in the long-slit spectra of Solf & Böhm (1993).

This work		Dist (″)	$< V >$ (km/s)	L[O I] ($10^{-4}L_\odot$)	SB93	Dist (″)	$< V >$ (km/s)
1st peak	HVB	0.12	−190	11.6	C[a]	0.20	−180
	LV	0.13	−50	11.3	A[a]	0.11	−43
extension	HVB	1.0	−320	1.9	C[a]	0.52	−340
	LV	1.4	−150	3.3			
bowshock	HVB[c]	2.7	−210	2.5	B1[b]	2–2.5	−255
jet end	HVB[c]	3.9	−190	0.4	B2[b]	3–3.5	−200
counter-jet	HVR	−1.0	+230	0.3			

[a] Parameters given in SB93
[b] Parameters estimated on [O I] P-V map of SB93
[c] Single gaussian fit

Table 1 summarizes global properties of the various features in the [O I] jet, namely the projected distance from the continuum, centroid velocities of fitted gaussian components, and dereddened luminosity in the [O I]λ6300 line (spatially integrated over the whole feature). We adopt a distance to DG Tau of 140 pc and A_V=3.2 (HEG95). We derive a total [O I] luminosity over the whole field of view of 3.5×10^{-3} $L_\odot$ and a dereddened R magnitude of 8.91. The corresponding equivalent width of [O I] is 10 Å, at the lower end of the range observed by HEG95 (11–22 Å). For comparison, Tab. 1 also compiles properties of the various features identified by SB93 in long-slit spectra.

In the following sections, we discuss in turn the intensity and velocity structure of the blueshifted jet, counter-jet, and halo, and the implications on the mass-loss process.

4. Blueshifted jet

4.1. Comparison with SB93 and proper motion estimates

The full variation of our line profiles along the jet axis is summarized in the form of a position-velocity (P-V) diagram in Fig. 4. The increase in velocity and line width out to ∼1″ , and their following decline out to the end of the jet, are reminiscent of the complex velocity gradients observed at higher spectral resolution by SB93. Using our gaussian decomposition of the line profiles, we may attempt a more precise comparison with the velocity features identified by SB93, and search for positional shifts suggestive of proper motions over the 2 year time interval between the two sets of observations.

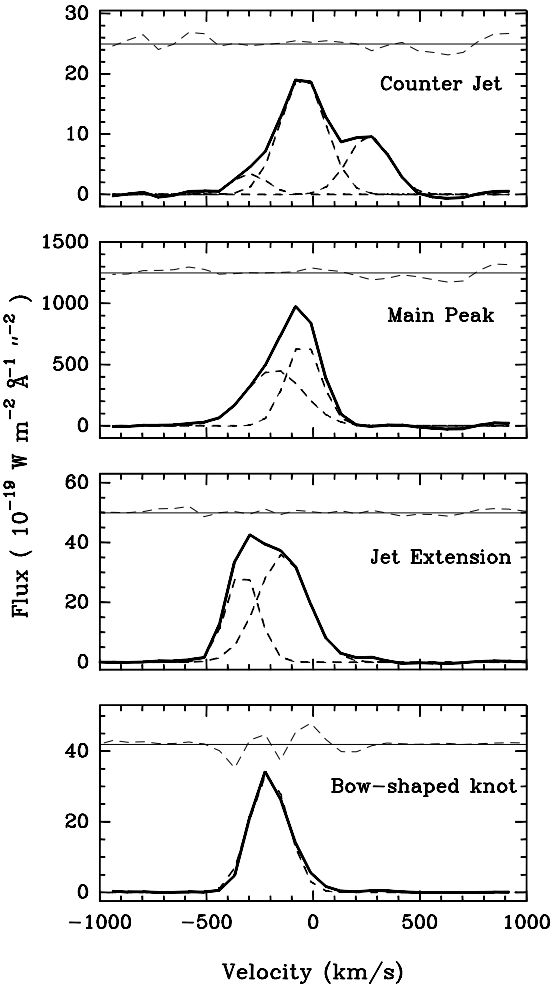

Fig. 3. Characteristic [O I] line profiles in regions identified in the [O I] map. Except for the main peak, where we show the peak lens spectrum, spectra have been averaged over 0.6″. We observe strong velocity gradients and line asymmetries. Our gaussian fits are shown as dashed lines and the corresponding residuals (multiplied by 3) are plotted at the top of each graph.

Based on their very similar velocity and position (Tab. 1), we identify the HVB component of our central peak with the innermost part of feature C of SB93, and the LV component of our central peak with feature A. Within our uncertainties in position (±0.05″) and velocity ($1\sigma \sim 20$ km/s), our observations are compatible with an essentially stationary (or only slowly varying) feature.

The HVB component in our jet-like extension corresponds well to the high velocity part of feature C from SB93, although maximum velocity (−320 km/s) seems to be reached at a slightly larger distance than in SB93 (0.7″ instead of 0.5″). We cannot tell whether this small shift is real or results from our low spectral resolution failing to resolve the gradient close to the strong main peak. Similarly, the LV component along our jet-like extension presents some similarities with the accelerating blue wing of component A observed by SB93; however, maximum velocity is reached even further away (1.4″ compared with 0.22″ in [O I], 0.72″ in [S II] in SB93). In fact, our LV component is tracing the whole low-velocity wing of the line profile (cf. Fig. 3), and may include a broad range of emission unrelated to the wing of the narrow feature A observed by SB93. Given these various uncertainties, we do not attempt to derive proper motions for this complex region.

In contrast to the innermost [O I] peak, substantial proper motions are most likely present in the outer two knots. Recently, Eislöffel (1992) estimated tangential velocities of 100–160 km/s for [S II] knots in images of DG Tau (distances from 2.5″ to 8.7″). Applying the proper motion of 0.145″/yr (103 km/s at 140 pc) derived by Eislöffel for his innermost knot (ejection date 1970), we find that it should lie at the date of our observations at $\sim 3.7''$ from the star, that is, very close to our faint jet terminal peak. At the date of SB93 observations (August 1992), the same knot would be located at $d \sim 3.3''$ i.e. at the tip of the outermost component of their feature B (hereafter knot B2). As our derived terminal velocity −190 km/s is very similar to the centroid velocity of knot B2 (Table 1), we identify B2 with our jet termination region and confirm its rather high proper motion of ∼ 100–150 km/s as estimated by Eislöffel (1992). We similarly identify our bow-shaped knot with the higher velocity peak of feature B from SB93 (hereafter knot B1); assuming similar proper motion, the bow-shaped knot would lie at the date of SB93 observations at $d \sim 2.3''$, that is, right at the tip of knot B1. The similar centroid velocities reinforces this cross-identification.

Our observations are thus compatible with the innermost bright peak beeing stationary, while the outermost knots, at distances of 2.7″ and 4″ from DG Tau, would possess roughly constant outward proper motion of ∼100 km/s.

4.2. Transverse morphology and velocity gradients

Channel maps indicate an increase in jet width with decreasing velocities, mostly apparent towards the bow-shaped knot. We investigate this effect in more detail in Fig. 5, where we represent the variation of line shape with transverse distance to the jet axis, across the jet-like extension and the bow-shock regions. For illustrative purposes, we also plot centroid velocities derived from our gaussian fits.

In both cases, the highest velocities are encountered towards the jet axis, while profiles at large distances ($> 1.3''$) peak at lower velocities (below −50 km/s). In the jet-like extension, the profile shape suddenly changes at ± 0.75″ from the jet axis: Closer to the axis, line profiles are very broad and are best accounted for by two gaussian components with centroids at −320 km/s (HVB) and ≃ −150 km/s (LV). No velocity gradient is apparent in either component on such spatial scales. At distances greater than 0.75″ , spectra have much lower velocities, with centroids around −50 km/s and a faint blue wing. Such profiles probably arise from a combination of both the halo and PSF wings from the main emission peak spectra (see Sect. 6). In contrast, in the bow-shaped knot region, a continuous transverse gradient in centroid velocity is observed out to at least 1″ from

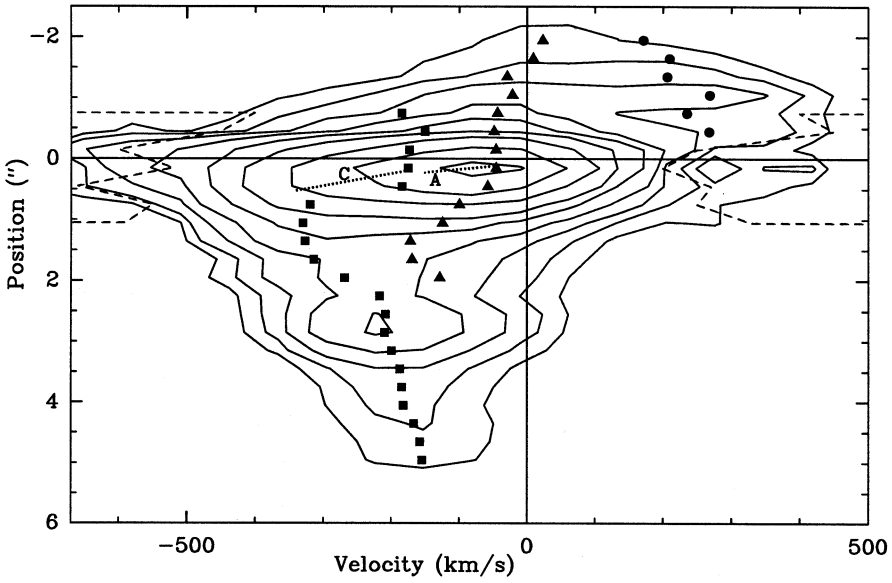

Fig. 4. Position-velocity diagram along the jet. Spectra are sampled every 0.3″ along the jet and averaged over a width of 1″ perpendicular to the jet axis. Centroid velocities derived from our gaussian fits are plotted for the HVB (squares), LV (triangles) and HVR (circles) whenever considered reliable (see text). Dashed lines outline regions close to the star where the emission drops below 3 times the local photon spectral noise. Dotted lines illustrate the velocity gradients observed in features A and C of Solf & Böhm (1993). Intensity contours decrease by factors of 2 starting at 83 % of the peak.

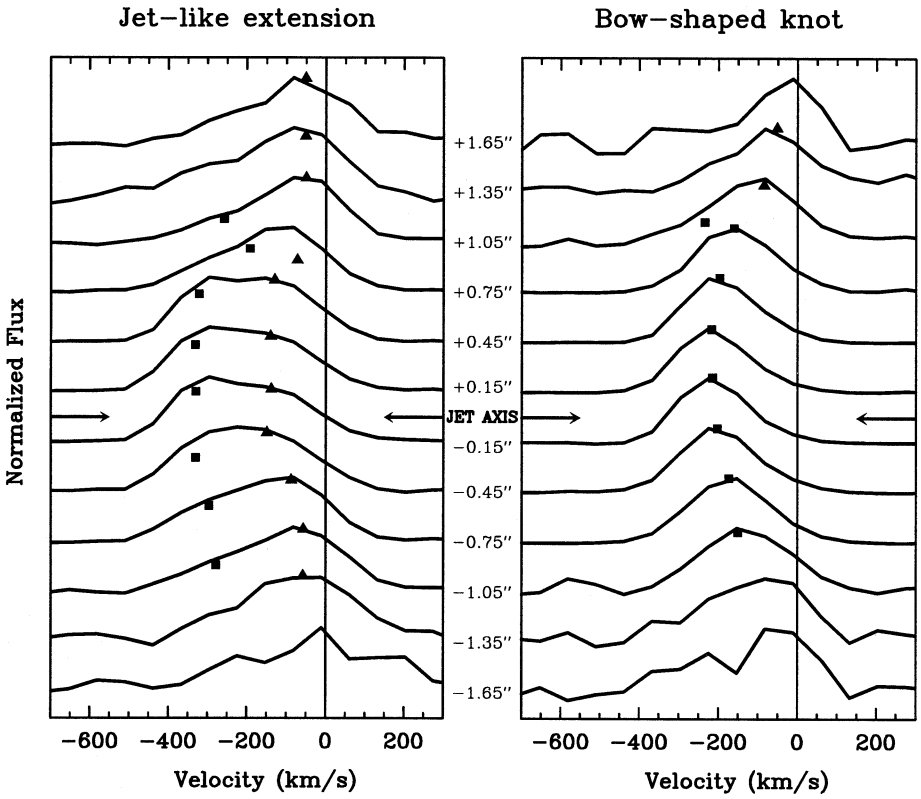

Fig. 5. Variation of the line profile perpendicular to the jet axis in the jet-like extension and the bow-shaped knot. Spectra are sampled every 0.3″ transverse to the jet and averaged over a width of 1″ along the jet. Distance to the jet axis is indicated in the center. Centroid velocities derived from our gaussian fits are also shown for the HVB (squares) and LV (triangles) components whenever considered reliable (see text).

jet axis. It is not until distances of 1.35″ that centroid velocities become lower than −100 km/s, and spectra start resembling the halo spectral profile (see Sect. 6). We conclude that the observed velocity decrease from −230 km/s to −120 km/s over a transverse distance of ± 1″ is intrinsic to the bow-shaped knot emission. Such an extended transverse gradient is characteristic of the wings of a bow-shock (see e.g. Wilkin 1996).

We also investigate the width of the jet at several distances from the star, using transverse intensity cuts. We consider two velocity channels at −295 km/s and −150 km/s, close to the centroids of the HVB and LV gaussians in the jet-like extension. Analysis is performed on raw channel maps, where we have a robust estimate of the FWHM for unresolved structures (0.75″ ± 0.05″) derived from both the continuum and the main [O I] peak (for which SB93 reported a width < 0.1″).

The jet remains unresolved out to distances of ∼ 0.4″ from the star. Subtracting our nominal PSF in quadrature indicates intrinsic FWHM ≤ 0.35″ (3σ), comparable with the upper limit

from the deconvolved image. At distances between 0.8″ and 1.4″ from the star (jet-like extension) the measured FWHM increases up to 0.9–1.1″ . However, transverse intensity cuts are no more well fitted by a single gaussian, and show broad extended wings beyond 0.75″ from the jet axis that, as we showed above, correspond to profiles dominated by the halo and the PSF of the main peak. When a separate gaussian fit to these wings (FWHM ∼1.8″ , intensity ≤ 30% of total intensity on the jet axis) is subtracted from the transverse intensity profile, the net resulting FWHM for intrinsic jet emission is only 0.83± 0.05″ and 0.87 ± 0.03″ for the HVB and LV channels[1], showing that the jet-like extension is in fact only marginally resolved in the transverse direction (intrinsic width ≤0.6″). Across the bow-shaped knot, all spectral channels are resolved with FWHM increasing with velocity (nominal width varying from 0.7″ to 1.58″ for velocities ranging from −295 km/s to −10 km/s). The main peak PSF and halo contribution have negligible effect there. Our nominal upper limits on the jet size (FWHM ≤ 0.35″ at 0.4″) and full opening angle (≤ 25° at 1.1″) are compatible with FWHM sizes ≃ 0.25–0.3″ and full opening angles of 1°–10° found by Ray et al. (1996) in HST observations of the HH30 and HL Tau jets.

4.3. Discussion

We have shown that the DG Tau jet displays a complex morphology, with at least 3 distinct knots between 0.15″ and 4″ from the star. We now use the two-dimensional intensity and velocity information brought by our data, combined with proper motion estimates and previous line ratio information (SB93), to propose possible origins for these various structures, investigate the time variability of the ejection, and improve mass-loss rate estimates.

The outer knots

The most popular explanation at present for the origin of knots in stellar jets is the presence of shocks in the jet flow (see e.g. Raga 1993 for a review). Several kinds of shocks can be distinguished: steady recollimation shocks (Falle et al. 1987), internal oblique shocks due to jet instabilities (Rossi et al. 1997; Stone et al. 1997), internal jet working surfaces caused by time variability in the ejection velocity or direction (e.g. Raga et al. 1990; Raga & Biro 1993; Biro & Raga 1994). In the latter cases, sideways ejection of matter from the jet beam and/or jet bending drive curved shocks (similar to "bowshocks") into the ambient gas causing local entrainment.

The properties of the outermost knots in the jet of DG Tau favor an interpretation in terms of working surfaces: The knot at 2.7″ from the star exhibits a curved morphology (Fig. 1) and a marked transverse velocity decrease (see Fig. 5) strongly suggestive of a bowshock driven into the ambient medium. The large proper motion of the two knots (∼ 100 km/s) is also consistent with a working surface nature.

This interpretation is further supported by the presence of [N II], Hα, and [S II] emission in these two outer knots (SB93). The relatively high excitation level needed to excite [N II] and Hα is not expected in oblique shocks resulting from jet instabilities, but it can be easily reached at the apex of an internal working surface. For example, in the case of internal working surfaces created by a periodic jet velocity variability, Raga & Kofman (1992) have shown that shock speed asymptotically decreases inversely with distance d from the source as $V_{sh} = V_{ws}^2 \Delta\tau / 2d$ where V_{ws} is the working surface advance speed, $\Delta\tau = \Delta x / V_{ws}$ the period of variability, and Δx the separation between successive working surfaces. For the outermost two knots in DG Tau, we would obtain $\Delta\tau \sim 8.5$ years (from the projected separation of 1.3″ and tangential proper motion of 103 km/s), and shock speeds $V_{sh} \sim 40$ and 25 km/s for B1 and B2 respectively (corrected for an angle of 51° to the plane of the sky (Eislöffel 1992)), sufficient to excite [N II] and Hα. These estimates are only illustrative, as the asymptotic regime may not apply so close to the star. Spatially-resolved line ratios are required to further constrain the shock parameters.

Jet-like extension

This feature is striking by its collimation (length to width ratio of 1.4″/0.5″ ∼ 3), its apparently smooth brightness distribution (we observe a roughly exponential decline), and strong velocity increase from 0.15″ to ∼1″ from the star. In addition, the HVB component in this region shows a notable absence of [S II] emission, indicating a higher density than in all other features (SB93).

An attractive explanation would be that the dense HVB component in the jet-like extension is tracing the true jet flow, and that its velocity increase results from the same time dependence of ejection velocity that created the outermost two knots (see above); Raga et al. (1990) showed that in a variable velocity jet, ramps of increasing velocity with distance are naturally produced, separated by velocity discontinuities giving rise to working surfaces. The fact that we only observe the first ramp may result from the drop in density in the following flow segments, where more material has been "swallowed" by the internal working surfaces (see e.g. Raga & Kofman 1992). One would expect to find a working surface close to the end of the "accelerating" jet flow, i.e. ∼ 1–1.5″ from the star. Detection by SB93 of [N II] emission at d ∼1" and V∼ −300 km/s, roughly agrees with this expectation. We cannot however at this point rule out other possible origins for the velocity increase, such as for example MHD acceleration of the jet flow just beyond the Alfvén surface, at $d/r \sim 1 - -10$ (Ferreira 1997). This would imply substantial jet expansion, but at scales not currently resolved. A definitive test of the variable velocity hypothesis would be kinematic evolution of this structure over timescales of order $\Delta\tau \sim 8$ years.

Another notable feature of the jet-like extension is the presence along its length of lower velocity emission with estimated centroids ranging from −50 to about −180 km/s; [S II] emission is detected at these velocities (SB93), implying substantially

[1] uncertainties around the mean value refer to the rms dispersion (1σ) among measurements at 4 independent positions

lower densities than in the HVB component discussed above. Hence SB93 proposed that the component at −50 km/s traces a slow disk wind of distinct origin from the fast jet. Our observations show that both LV and HVB components have a similar collimated morphology and apparent acceleration out to 1–1.5″ from the star. Thus, an alternative explanation would be that at least some of the slower, [S II]-strong emission arises in an entrained layer around the fast, dense [O I] jet. A previous example of a low-velocity component co-existing with a fast jet is HH 47 (Hartigan et al. 1993). Recent HST images reveal that the slow gas is entrained in a series of small bowshock wings (Heathcote et al. 1996), and a similar situation could possibly occur in the jet of DG Tau; alternatively, some entrainment might also take place in a viscous boundary-layer (Cantó & Raga 1991).

We point out that the −50 km/s component in DG Tau is an exception among cTTS studied at high resolution, which have low velocity components peaking at much lower speeds ∼ –10 km/s (HEG95). An entrainment interpretation is consistent with this rarity, since DG Tau also possesses the strongest jet and densest circumstellar environment among that sample[2]. A test of our proposed interpretation awaits higher resolution observations, providing reliable proper motion estimates and fully resolved structure transverse to the jet.

Main emission peak and jet mass-loss rate

The innermost, unresolved [O I] peak does not show significant proper motion, suggesting that it does not arise from a moving working surface but rather from a steady region in the jet flow where emissivity is enhanced. Its projected distance from the star, $d \sim 0.15''$ = 21 AU, is comparable to or greater than the jet radius at this point (for which our deconvolved map gives an upper limit of $r \leq 0.18''$). This apparently argues against heating by ambipolar diffusion (Safier 1993) or oblique shocks against a flared disk surface (Hartmann & Raymond 1989), which are predicted to occur closer to the disk plane. An interesting alternative is heating by the jet recollimation shock. Ouyed & Pudritz (1993,1994) investigated forbidden line profiles from recollimation shocks in magnetic disk winds, and derived for DG Tau a projected distance of 25 AU for the "focal point" (cf. Gomez de Castro & Pudritz 1993), indeed very close to our observed 21 AU. However, the [S II] to [O I] ratio is predicted to be the same in the LV and HVB components, in contrast with observations (SB93; see also Hirth et al. 1994). Hence the dominant heating mechanism in the inner knot is still unclear.

As discussed in Appendix A of HEG95, the uncertainty in heating mechanism causes a corresponding uncertainty in the derived jet mass-loss rate; in the case of distributed heating, e.g. by ambipolar diffusion, the emission scale is the beam size, while in the case of a single unresolved shock-front, the relevant scale is the cooling length. Inferred values differ by a factor of 100 for [O I]λ6300 observations in a 1.25″ slit, and range in DG Tau from 3×10^{-7} to 3×10^{-5} $M_\odot$/yr (HEG95).

Our higher resolution observations show that most of the [O I] flux from DG Tau comes in fact from the innermost knot, of size $\leq 0.4''$. In addition, our aperture photometry leads to an [O I] luminosity of 1.1×10^{-3} $L_\odot$ for the HVB component in the knot, lower by a factor 5 than that adopted by HEG95. We then use the two methods outlined in appendix A of HEG95 to derive revised estimates of the mass-loss rate. In the case of distributed heating, we adopt a transverse flow velocity of 150 km/s (radial velocity of −190 km/s corrected for an angle of 51° to the plane of the sky; Eislöffel 1992) and an emitting size scale of 0.4″. If we adopt the same electron density as HEG95 (7×10^4 cm^{-3}) the derived mass-loss rate is 1.9×10^{-7} $M_\odot$/yr. However, given the non-detection of [S II] in the HVB at this position (SB93), electron density could be closer to the critical density of the [O I] line, leading to a mass-loss rate of only $\sim 1.3 \times 10^{-8}$ $M_\odot$/yr. In the case of a single shock front, adopting a full jet velocity of 250 km/s and a shock velocity of 30 km/s, we derive a value of 6.5×10^{-6} $M_\odot$/yr. Thus, while our data do not resolve the ambiguity, the range of mass-loss rates for DG Tau is now shifted to 5 to 25 times lower values.

5. The red counter-jet

The high-velocity red channel map of [O I] emission (rightmost panel of Fig. 2) provides the first image of the counter-jet in DG Tau and allows some quantitative study.

The intensity distribution of the counter-jet may be used to constrain the spatial extent of the circumstellar disk around DG Tau. A distinct red-shifted component with peak above 5σ is not detected until distances of $\sim 0.45''$ from the continuum. The projected radius ∼ 70 AU inferred for the occulting structure is slightly lower than the projected outer disk radius of 90–150 AU derived from mm interferometric imaging of DG Tau (Dutrey et al. 1996). At $\sim 1''$ from the star, the redshifted jet is well detected, and is only ∼10 times weaker than the blueshifted jet at the same distance from the star. Assuming a rough intensity symmetry between the two sides of the jet, we infer a modest relative extinction $A_V \simeq 3$ mag. With the disk radial surface density law derived from the mm interferometric observations of Dutrey et al. (1996), the optical extinction would be larger than 150 mag at 1″. The counter-jet detection at 1″ thus suggests a sharp disk outer edge within a projected radius of 150 AU. The subsequent fall off in counter-jet intensity beyond 1.5″ to the north-east may not be real, as only one of the individual exposures has imaged this edge of the field and spectra there have a lower S/N ratio as well as more uncertain flat-field correction.

Average velocity of high-velocity emission in the counter-jet at 1″ is ≃ +230 km/s, 1.4 times lower than in the blueshifted jet at the same distance (−320 km/s). The counter-jet appears to decelerate further out (Fig. 4). Such mild asymmetries are common in jets from TTS (Hirth et al. 1994). The counter-jet also appears less well collimated than the blueshifted jet (Fig. 2). However, contamination by the halo is proportionately more

[2] The very low velocity component typical of TTS is still present in DG Tau at −19 km/s, as best seen in [O I]λ5577 spectra (Fig. 14 of HEG95). The long-slit spectrum of SB93 indicates that it is much more compact than the faster LV and HVB velocity components investigated in this study, and not significantly displaced from the continuum position, consistent with a different physical origin.

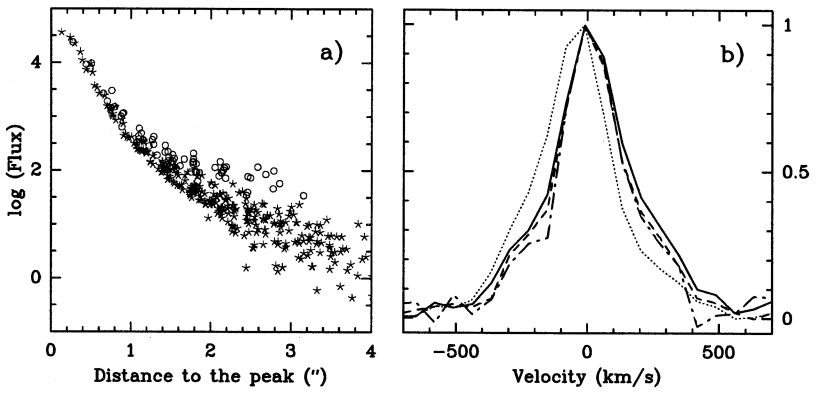

Fig. 6. a Comparison of the radial fall-off of the continuum (asterisks) and the main peak [O I] integrated fluxes (circles). Only lenses outside the jet and counter-jet regions have been included. Both curves are normalized to their maximum intensity and shown on logarithmic scale. **b** Characteristic spectrum of the halo. Average spectra from south-east and north-west quadrants *after* subtraction of the [O I] peak spectrum PSF for distances to the main [O I] peak greater than 1″(solid line), 1.5″(dashed line) and 2″(dotted-dashed line); in dotted line, the average profile for distances $\geq$ 1″*before* subtraction of the PSF (*hybrid spectrum*). All spectra are normalized to their maximum intensity.

important here than in the much brighter blue jet, and prevents us from deriving a reliable intrinsic width.

6. The low velocity halo

As pointed out in Sect. 3.1, regions well outside the jet show an excess of [O I] emission compared with the continuum, indicative of a weak [O I] halo. To investigate its structure, we now restrict ourselves to the south-east and north-west quadrants of DG Tau, in order to exclude jet and counter-jet contamination.

We compare in Fig. 6a the radial fall-off of the continuum and main [O I] peak integrated fluxes. The [O I] surface brightness is clearly dominated by the PSF of the unresolved main peak out to d$\sim$0.9″ ; beyond this point, [O I] flux drops less rapidly than the continuum, and the line to continuum ratio increases by up to a factor two at d $\simeq$ 1.5″ . Centroid velocities of the LV component, derived from gaussian fits to individual line profiles, remain roughly constant around $-$40 km/s up to d$\simeq$ 0.9″ and then increase to less negative values (up to 0 km/s) at larger distances.

Fig. 6a shows that the contribution of the PSF wings of the main [O I] peak is still substantial at distances $\geq$ 1 ″ ($\simeq$ 50% at 1.5″). In order to isolate the characteristic spectrum of the halo, we thus subtract from each individual spectrum the main [O I] peak profile scaled according to the PSF fall-off at the corresponding distance. We compare in Fig. 6b average spectra after subtraction of the PSF component for varying distances to the [O I] peak. The three halo spectra agree remarkably: they are centered at 0 km/s, broad (FWHM $\simeq$ 400 km/s) and symmetric. We also show for comparison the average spectrum (for distances $\geq$ 1″) before PSF subtraction, which we refer to as *hybrid* spectrum since it results from a combination of the [O I] peak and halo profiles. The evolution in the LV centroid velocity away from the [O I] peak corresponds to the transition from [O I] peak-dominated to halo-dominated spectra.

The presence of a low-velocity halo in [O I] is quite intriguing. A first possible origin could be in-situ [O I] emission in a wide flow of much lower collimation than the jet: For example a molecular flow entrained by jet working surfaces (e.g. Raga & Cabrit 1993), or an intrinsic wide-angle magnetic wind, in which the jet would merely trace the denser axial regions (Shu et al. 1995). However, a molecular outflow should be accelerated near the jet working surfaces, while the wide-angle wind proposed by Shu et al. (1995) would be expected to undergo similar outward velocity gradients as those observed on-axis (cf. Fig. 4). The lack of velocity gradients in the halo is therefore difficult to explain, unless there is complete dynamical decoupling between the wide flow and jet regions beyond 0.2″ of the star.

Another process that could account for the halo is scattering on surrounding circumstellar dust. As [O I] emission is formed higher up above the disk plane than the continuum, we could expect a more efficient scattering of [O I] line photons, due to blocking of the continuum light by the circumstellar disk. The line/continuum ratio would then increase with distance from the star without a significant profile change. Velocities centered around 0 km/s could be produced by scattering of emission from both the blue and red sides of the wind. Detailed modeling is under way (Ménard et al., in preparation) to see whether differential scattering is sufficient to reproduce the magnitude of the observed halo, or whether in-situ emission is required.

7. Conclusions

We have presented the first sub-arcsecond scale 3D spectro-imaging observations of [O I]λ6300 emission in DG Tau. From a combined morphological and kinematical study, we derive the following main results:

- Blueshifted [O I]λ6300 emission is confined to a collimated outflow elongated along PA=222°, confirming the blueshifted jet inferred from long-slit spectra (SB93). The deconvolved image reveals a complex morphology consisting of a bright unresolved peak at $\sim$ 0.17″ from the star, a collimated jet-like extension out to 1.5″ , a separate knot at 2.7″ with a distinctive bow shape, and a faint resolved terminal knot at $\sim$ 4″ .
- The separate resolved emission knot at 2.7″ shows a curved morphology, high proper motion and transverse velocity gradient suggestive of a bowshock structure. The faint outer terminal knot is well resolved transverse to the jet and has similar proper motion. We therefore propose that the two outer [O I] emission knots arise from working surfaces in a time-dependent outflow. The higher line excitation toward

the outer knots (e.g. in [N II], SB93) qualitatively supports this suggestion. Inferred variability timescale is $\Delta t \simeq 8.5$ yr.

- The jet-like extension is only marginally resolved transverse to the jet axis and corresponds to a steep ramp of increasing high centroid velocities reaching -340 km/s at 0.5–0.7″ from the star (feature C of SB93). Such a ramp could result from the velocity variability creating the bowshocks, or from MHD acceleration. Determination of the exact nature of this feature awaits higher angular resolution or third epoch observations. The corresponding low-velocity component, though less dense (SB93), follows the spatial and velocity behavior of the high velocity part of the profile. We propose that it arises from entrained matter along the walls of the fast jet.
- The bright unresolved central peak might arise in a stationary structure, possibly linked to jet collimation, $\sim$ 20 AU from the star. Our aperture photometry and size constraint lead to revised estimates of the jet mass loss rate in DG Tau: between $1.3–19\times10^{-8}$ $M_\odot$/yr for distributed heating and 6.5×10^{-6} $M_\odot$/yr for a single shock front, thus reducing previous estimates by a factor 5 to 25.
- We unambiguously detect the red counter-jet of the system out to 1.5″ from the star. It is attenuated below detection within 0.45″ of DG Tau but well detected at $\geq 1''$, suggesting that the occulting circumstellar disk observed in mm interferometry may be truncated within a projected radius of 150 AU. Velocity $\sim$ +230 km/s is slightly lower than in the blueshifted jet.
- Our observations reveal a faint halo of extended [O I] emission roughly symmetrical about DG Tau, with a broad profile peaking at $\sim$ 0 km/s. Modelling is under way to determine whether it can be explained by enhanced dust scattering, or if in-situ emission is required.

Acknowledgements. We are grateful to S. Edwards, J. Eislöffel, and A. Raga for helpful suggestions, and to the referee, J. Solf, for critical comments that led to significant improvement of the paper. Claudia Lavalley acknowledges a scholarship from DGAPA (Universidad Nacional Autonoma de Mexico).

References

Appenzeller, I., Jankovics, I., Ostreicher, R. 1984, A&A, 141, 108
Bacon, R., Adam, G., Baranne, A., Courtes, G., Dubet, D., Dubois, J. P., Emsellem, E., Ferruit, P., Georgelin, Y., Monnet, G., Pecontal, E., Rousset, A., Say, F. 1995, A&AS, 113, 347
Bevington, P.R., 1969, Data Reduction and Error Analysis in Physical Sciences, Mc Graw Hill
Biro, S., Raga, A. C. 1994, ApJ, 434, 221
Böhm, K. H., Solf, J. 1994, ApJ, 430, 277
Cabrit, S., Edwards, S., Strom, S. E., Strom, K. M. 1990, ApJ, 354, 687
Cantó, J., Raga, A. C. 1991, ApJ, 372, 646
Dutrey, A., Guilloteau, S., Duvert, G., Prato, L., Simon M., Schuster, K., Menard, F. 1996, A&A, 309, 493
Edwards, S., Cabrit, S., Strom, S. E., Heyer, I. 1987, ApJ, 321, 473
Edwards, S., Cabrit, S., Ghandour, L., Strom, S. 1989, in *ESO Workshop on Low Formation and Pre-Main Sequence Objects* ed. B. Reipurth (Garching:ESO), p.385
Edwards, S., Ray, T., Mundt, R. 1993 in *Protostars & Planets III* ed. E. Levy & J. Lunine (Univ. Arizona Press), p.567
Eislöffel, J. 1992, PhD thesis, Universität Heidelberg
Falle, S.A.E.G., Innes, D.E., Wilson, M.J. 1987, MNRAS, 225, 741
Ferreira, J. 1997, A&A, 319, 340
Gomez de Castro, A. I. & Pudritz, R., 1993, ApJ, 409, 748
Hartigan, P., Morse, J.A., Heathcote S., Cecil G. 1993, ApJ, 414, L121
Hartigan, P., Edwards, S., Gandhour, L. 1995, ApJ, 452, 736 (HEG95)
Hartmann, L., Raymond, J. C. 1989, ApJ, 337, 903
Heathcote, S., Morse, J.A., Hartigan, P., Reipurth, B., Schwartz, R.D., Bally, J., Stone, J.M. 1996, AJ, 112, 1141
Hirth, G. A., Mundt, R., Solf, J. 1994, A&A, 285, 929
Jankovics, I., Appenzeller, I., Krautter, J. 1983, PASP, 95, 883
Kepner, J., Hartigan, P., Yang, C., Strom, S. 1993, ApJ, 415, L119
Kwan, J., Tademaru, E. 1988, ApJ, 332, L41
Kwan, J., Tademaru, E. 1995, ApJ, 454, 382
Ouyed, R., Pudritz, R. 1993, ApJ, 419, 255
Ouyed, R., Pudritz, R. 1994, ApJ, 423, 753
Raga, A. C. 1993, Ap&SS, 208, 163
Raga, A.C., Kofman, L. 1992, ApJ, 386, 222
Raga, A. C., Biro, S. 1993, MNRAS, 264, 758
Raga, A. C., Cabrit, S. 1993, A&A, 278, 267
Raga, A.C., Cantó, J., Binette, L., Calvet, N. 1990, ApJ, 364, 601
Ray T.P., Mundt, R., Dyson, J.E., Falle, S.A.E.G., Raga, A.C. 1996, ApJ, 468, L103
Rossi, P., Bodo, G., Massaglia, S., Ferrari, A. 1997, A&A, in press
Rousset, A. 1992, PhD Thesis, Univ J. Monnet de Saint-Etienne.
Safier P. 1993, ApJ, 408, 148
Shu, F.H., Najita, J., Ostriker, E.C., Shang, H. 1995, ApJ, 455, L155
Stone, J.M., Xu, J., Hardee, P.E. 1997, ApJ, in press
Solf, J. 1989, in *ESO Workshop on Low Mass Star Formation and Pre-Main Sequence Objects* ed. B. Reipurth (Garching:ESO), p. 399
Solf, J. 1994 in *Stellar and Circumstellar Astrophysics* ASP Conference Series, p. 57
Solf, J., Böhm, K.H. 1993, ApJ, 410, L31 (SB93)
Wilkin, F.P., 1996, ApJ, 459, L31

This article was processed by the author using Springer-Verlag LaTeX A&A style file *L-AA* version 3.